Effect of Heat Treatment on Microstructure and Residual Stress of GH3536 Superalloy Fabricated by Selective Laser Melting

Guowen Qiao, Bi Zhang, Qian Bai ⓘ, and Yuvasheva Dilnoza

Widely applied in the aeronautic and aerospace industries, Ni-based superalloy GH3536 has outstanding strength and oxidation resistance at elevated temperatures. In this study, GH3536 specimens are fabricated by selective laser melting (SLM) followed by heat treatment (HT). The microstructure, residual stress, tensile strength, and hardness of both the SLMed and SLM-HTed specimens are investigated. Experimental results demonstrate that the SLMed specimens possess a supersaturated solid solution state due to the rapid cooling, and residual tensile stress exists in the subsurface periodically along the building direction. After heat treatment, Mo-rich carbides precipitate from the matrix, reducing the degree of solid solution. In addition, residual tensile stress caused by SLM converts to compressive stress due to heat treatment, and the periodic distribution of subsurface residual stress disappears. The study concludes that the heat treatment retards the solid solution strengthening and grain boundary strengthening of the SLMed specimens, resulting in a decrease in hardness and yield strength and a 53% increase in fracture elongation. This study can provide guidance to the application of SLMed GH3536 Ni-based superalloys.

1. Introduction

Additive manufacturing technology can fabricate components with complex shaped geometry and shorten the manufacturing cycle of product designs (Ref 1). Selective laser melting (SLM) is a typical additive manufacturing technology which has been successfully applied to various materials, such as stainless steel (Ref 2), aluminum alloys (Ref 3), and Ni-based superalloys (Ref 4). GH3536 (Hastelloy X) is a Ni-based solid solution strengthened superalloy with outstanding oxidation resistance and high-temperature strength, which has been applied to the hot end components of gas turbines (Ref 5). Therefore, the SLM technology of complex high-performance GH3536 Ni-based superalloy part has a broad application prospect in aeronautic, transportation and other high-end equipment.

In conventional GH3536 manufacturing processes, such as casting or forging, the material undergoes a slow heating and cooling, in which the coarse carbides in the matrix normally fully precipitate (Ref 6). Therefore, solid solution treatment is often required to improve the mechanical properties (Ref 7). Compared with conventional manufacturing processes, the rapid melting and solidification in SLM cause the solute trapping (Ref 8) and thus generate the supersaturated solid solution (SSSS) in the SLMed material (Ref 9, 10). This unstable SSSS could precipitate Cr and Mo carbides excessively at an elevated temperature in the service conditions, resulting in the deterioration of the mechanical properties (Ref 11). Therefore, it is of importance for GH3536 to be heat treated after SLM to stabilize the microstructure and maintain the material properties at the working condition. Several studies have been reported on the heat treatment of GH3536 fabricated by SLM. Tomus (Ref 12) and Marchese (Ref 13) heat treated the SLMed Hastelloy X specimens at 1,175 °C and found that the microscopic dendritic structure dissolved and a large amount of Mo-rich M_6C-type carbides precipitated. Keshavarzkermani (Ref 14) set the solution heat treatment temperature as 1177 °C and discovered that the yield strength after heat treatment was much lower than that of SLMed ones, leading to a higher strain hardening rate in the heat treated (SLM-HTed) specimens. The current studies of SLM-HTed parts generally focused on the microstructure evolution (Ref 13, 15) and the corresponding mechanical properties (Ref 16). However, the rapid heating and cooling during SLM lead to residual stress (Ref 17, 18). Especially, the tensile stress in the surface of SLMed parts may cause microcracks and thus deteriorate the fatigue performance. Therefore, it is also essential to study the evolution of residual stress in SLM-HTed parts. In this paper, heat treatment was conducted on the GH3536 SLMed specimens, and the microstructure, residual stress and mechanical properties before and after heat treatment were investigated.

Guowen Qiao and **Qian Bai**, Key Laboratory for Precision and Non-traditional Machining Technology of Ministry of Education, Dalian University of Technology, Dalian 116024, China; **Bi Zhang**, Department of Mechanical and Energy Engineering, Southern University of Science and Technology, Shenzhen 518055, China; **Yuvasheva Dilnoza**, School of Materials Science and Engineering, Dalian University of Technology, Dalian 116024, China. Contact e-mail: baiqian@dlut.edu.cn.

2. Materials and Experimental Procedure

Spherical GH3536 powders were prepared by the gas atomization method in argon gas. The powder size distribution and morphology are shown in Fig. 1. The average diameter of the powders was 30.2 μm. The chemical composition of the powders is shown in Table 1. The powders were dried in a vacuum oven at a temperature of 100 °C for two hours prior to the SLM experiment.

The specimens were fabricated by SLM in the Sodick OPM 250L. The layer thickness was set at 40 μm, and the substrate preheating temperature was 80 °C. The laser was set at a power level of 250-450 W and a scanning speed at 500-2000 mm/s. The volume energy density (VED) was defined as $VED = P/(vht)$, where P is the laser power, v is the scanning speed, h is the hatch spacing of the adjacent laser paths, and t is the powder layer thickness. In Fig. 2a, at a VED of 39.06 J/mm^3, a large number of pores were generated due to lack of fusion. The relative density increased with the increase in VED and leveled off when the VED reached 71.43 J/mm^3. Severe balling spatter formation was formed at VED of 93.75 J/mm^3, which was attributed to the perturbation of the molten pool (Ref 19). The optimized VED with no obvious defects was 71.43 J/mm^3, which is shown by the pentagram symbol in Fig. 2a.

The process window of the GH3536 Ni-based superalloy in the SLM process was obtained as shown in Fig. 2b. With a high laser power and a low scanning speed, a higher relative density was obtained, but the manufacturing process efficiency was low since the forming speed was low. A large number of pores were formed in the samples with a low power and a high speed due to lack of fusion. At a high power and a high speed, the strong temperature gradient below the laser beam generated the Marangoni effect, which increased the melt pool depth, recirculated the melt flow, and led to balling effect (Ref 20). Therefore, according to Fig. 2a-b, a laser power of 400 W and a scanning speed of 1750 mm/s were determined as the optimized parameters for SLM, which has a higher forming efficiency under the premise of high density, as marked by the pentagram symbol in Fig. 2b.

The specimens were heated at 1175 °C for one hour, followed by water cooling. The specimens for microstructure observations were cut by a wire saw, subsequently mounted, ground and polished to obtain a smooth surface without scratches, and then they were electrolytically etched by 10% oxalic acid solution. The tensile specimens were prepared according to ASTM E8/E8M-13a small size specimen standard. Tensile tests were performed at a WDW-100 tensile tester. An ARAMIS-4M measuring system based on digital image correlation was utilized as an optical elongator to obtain true stress-true strain curves in the tensile tests. The microstructure and tensile fracture morphologies were observed using a FEI-Q45 SEM. A SUPRA-55 Field Emission Scanning Electron Microscope equipped with an Electron Backscatter Diffraction (EBSD) system was used to analyze the material texture. An Empyrean x-ray diffractometer (Co-target) was used to analyze the phase composition, with a measurement angle range of 35-130° in steps of 0.02°. The element distribution was measured by a JXA-8530F PLUS Electron Probe Micro Analysis (EPMA). The microhardness was measured by a Type MVS-1000Z Vickers hardness tester with test load of 0.2 kg and holding time of 15 s. The residual stress was measured in the surface and subsurface of the specimens by Electronic Speckle Pattern Interferometry (ESPI)-based hole drilling method. The measurement was carried out within a total depth of 0.3 mm and in steps of 0.02 mm.

3. Results and Discussion

3.1 Microstructure of Specimens Before and After Heat Treatment

Figure 3 shows the microstructure of the specimens before and after heat treatment. The cellular sub-grain structure with a size of 0.5 μm existed in the SLMed specimens. After heat treatment, the cellular sub-grain structure disappeared, and Mo-rich carbides with micron size were discontinuously distributed on grain boundaries and within the grains. The microstructure of the SLMed specimens was closely related to their solidification process. The cooling rate R_{slm} during the solidification can be calculated using (Ref 21):

$$R_{slm} = \left(\frac{a}{\varphi}\right)^{\frac{1}{b}} \tag{Eq 1}$$

for Ni-based alloys, a=50 μmKs^{-1}, b=0.33, the dendritic spacing φ of the SLMed specimens in this study was statistically calculated as:
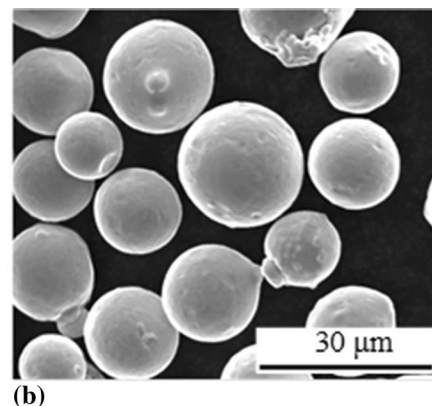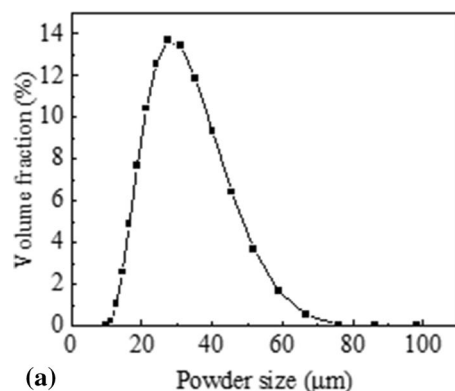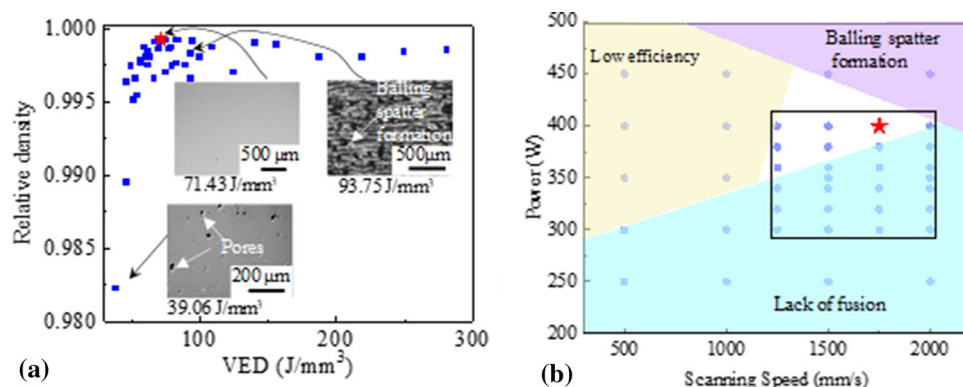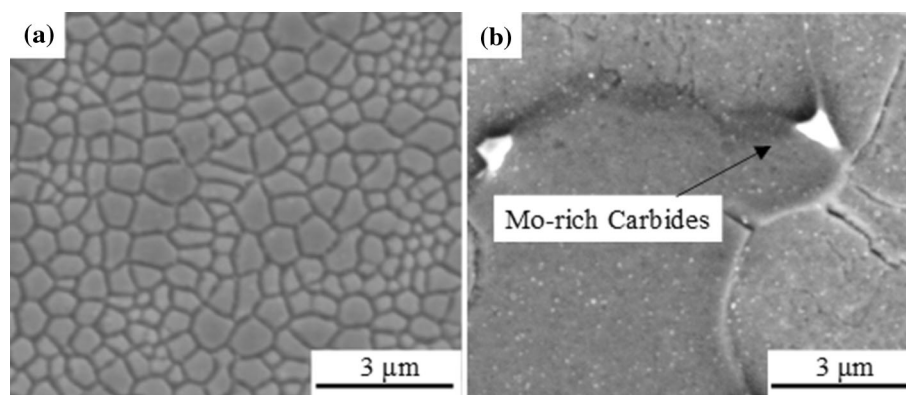

Fig. 1 (a) The powder size distribution, (b) SEM image of the powder of GH3536

Table 1 Nominal compositions of the powder GH3536 (wt.%)

Ni	Cr	Fe	Mo	Co	W	Si	C	Al	Mn	P	S	B
Bal.	22.52	19.36	9.46	1.60	0.74	0.33	0.07	0.05	0.03	0.034	0.003	0.002

Fig. 2 Process parameters optimization of GH3536 fabricated by SLM: (**a**) relative density, (**b**) process window

Fig. 3 SEM images of microstructure of (**a**) SLMed and (**b**) SLM-HTed specimens

$$\varphi = \left(N \cos\left(\frac{\pi}{6}\right) \right)^{\frac{1}{2}} \qquad (Eq\ 2)$$

where N (mm^{-2}) is the number of sub-grains per unit area, according to Fig. 3a, φ was 0.478 μm. The cooling rate of SLM R_{slm} was calculated as 1.14×10^6 Ks^{-1}, indicating that the SLM process can be considered as a rapid solidification process. Therefore, solute trapping (Ref 9) was accompanied in this SLM process, and a supersaturated solid solution was formed. After heat treatment, the carbides were precipitated from the supersaturated solid solution (Ref 13), as shown in Fig. 3b.

Figure 4a shows the secondary electron imaging (SEI) of the SLM-HTed specimens and Fig. 4b-f shows the corresponding EPMA mapping results. GH3536 is a Mo and Cr solution strengthening alloy. After heat treatment, Mo-rich carbides precipitated on grain boundaries and within the grains, but Cr-rich carbides were rarely found in this SLM-HTed material (Fig. 4b-f). It was attributed to the fact that Mo-rich carbides precipitate when the heat treatment temperature is higher than 870 °C (Ref 22). However, when a heat treatment temperature is below 745 °C, or when a slower cooling rate is used, the Cr-rich carbides precipitate (Ref 13). In this study, due to the heating temperature of 1175 °C and water cooling, Mo-rich carbides generated first during the cooling, which consumed a large amount of C element and inhibited Cr-rich carbide precipitation. In addition, due to the fast cooling rate, the Mo-rich carbides were preserved and further retarded Cr-rich carbide precipitation, so the precipitation phase in this study only consisted of Mo-rich carbides (Fig. 4e).

Figure 5 shows the result of EBSD analysis of the laser scanning surface before and after heat treatment. The SLMed specimen in Fig. 5a shows significant texture in the <001> direction before heat treatment, and texture extent was remarkably reduced after heat treatment (Fig. 5c). Fig. 5b and d shows the kernel average misorientation (KAM), identifying the areas of accumulated plastic deformation and increased geometrically necessary dislocations in the material (Ref 23). Significant plastic deformation was found in the SLMed material (Fig. 5b), and it was decreased after heat treatment (Fig. 5d). This was due to the fact that the SLMed specimen was fabricated by the layer-by-layer deposition, and each melt track underwent the cyclic thermal load, generating large number of plastic deformation areas. After the heat treatment, the dislocation
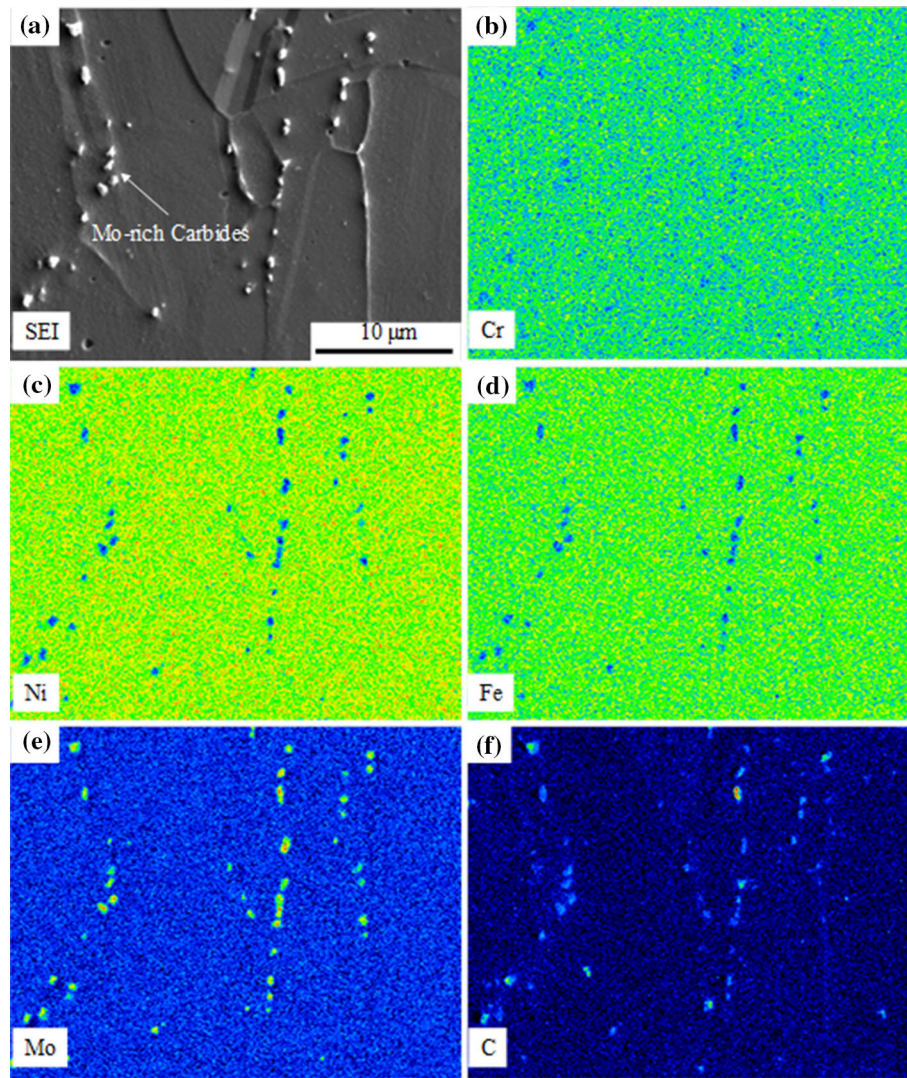
Fig. 4 (**a**) SEM image of SLM-HTed specimen, (**b-f**) EPMA element analysis for the area shown in (**a**)

annihilated (Ref 14), the sub-grains disappeared, and the annealing twins formed in the local areas (Fig. 5c). These processes consumed the strain energy within the grains, and thereby reduced the degree of plastic deformation of the material.

Figure 6 shows the x-ray diffraction (XRD) results of the powder, SLMed, and SLM-HTed specimens. Based on the extinction ratio of the material, these three specimens were mainly of the FCC structure, as shown in Fig. 6a. Carbides were not detected by XRD since the content was relatively low. In Fig. 6b, (111) diffraction peak was inconsistent with each state of the specimens, and the diffraction angle magnitude of the SLMed material was less than that of the powders and the SLM-HTed specimens. According to Bragg's law (Ref 16):

$$2d\sin\theta = n\lambda \qquad (Eq\ 3)$$

where θ is the diffraction angle, d is the interplanar spacing, n is a positive integer and λ is the wavelength of the x-rays. Therefore, the SLMed material had the largest interplanar spacing magnitude. This is due to the fact that solute trapping occurred in SLM, and more solute atoms were dissolved in the

matrix to form a supersaturated solid solution, leading to an increase in the interplanar spacing.

The micron-sized powders prepared by argon atomization can be considered stress-free. According to the XRD results, it can be seen that the diffraction peak in the SLMed material was shifted to the left by 0.153° with respect to that in the powder, indicating a large tensile stress. After heat treatment, the diffraction peak was shifted to the right by 0.257°, indicating a smaller tensile stress or even a compressive stress.

3.2 Residual Stress in the Surface and Subsurface of the Specimen

Figure 7a shows the residual stress in the surface and subsurface of the SLMed specimen before and after heat treatment by the ESPI-based hole drilling method. The hole drilling direction was parallel to the building direction of SLM, as shown in Fig. 7b. Residual tensile stress existed in the subsurface of the SLMed specimen and decreased along the depth direction, which was also found by Liu (Ref 24). The residual stress had a periodic distribution in the depth direction in each 40 μm interval, which was consistent with the powder layer thickness during the SLM process, as shown in Fig. 7b.
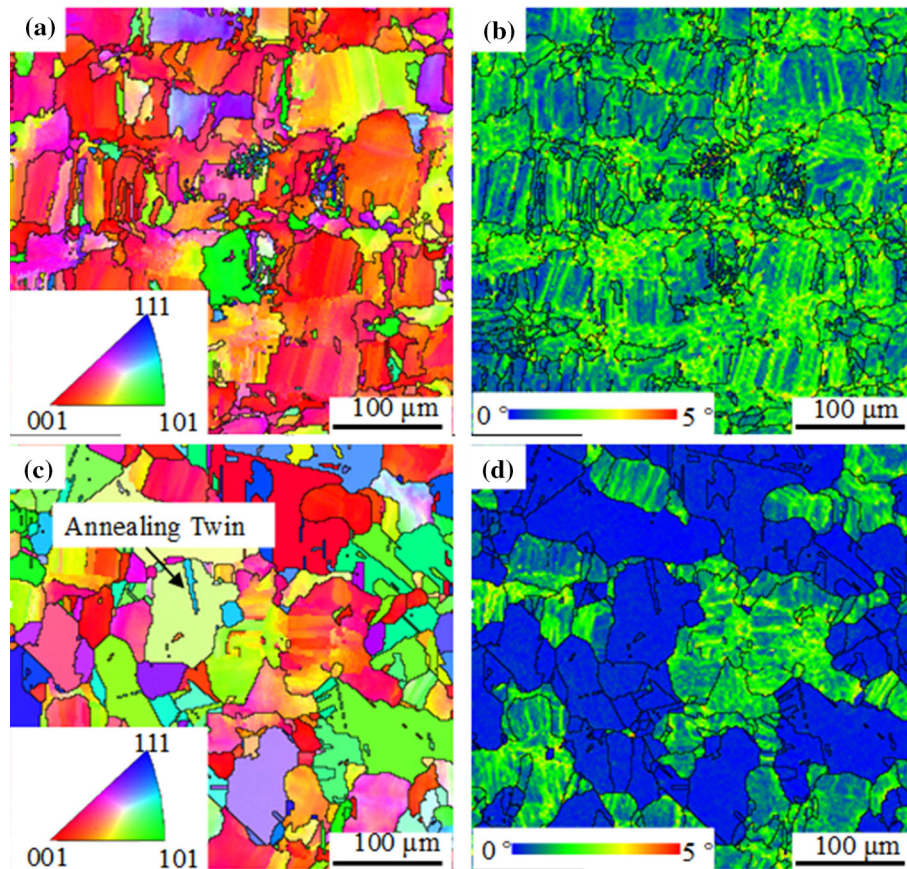
Fig. 5 (**a**) Inverse pole figure (IPF) and (**b**) kernel average misorientation (KAM) of SLMed material, (**c**) IPF and (**d**) KAM of SLM-HTed material on laser scanning surface
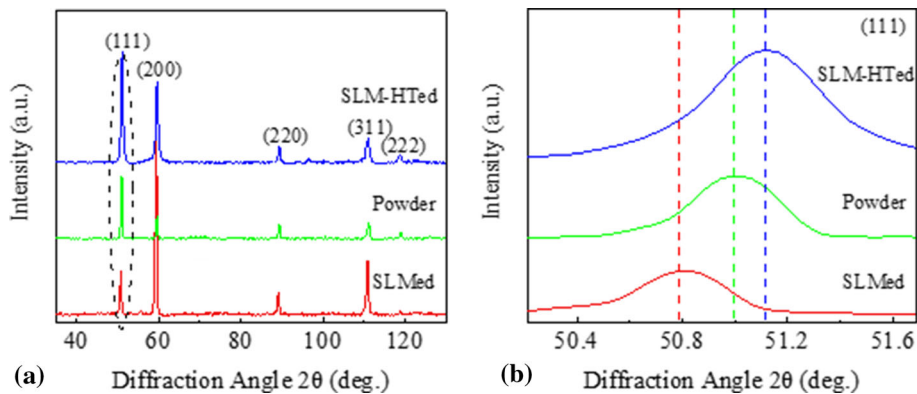

Fig. 6 (**a**) XRD results of the powder, SLMed and SLM-HTed specimens, (**b**) the enlarged partial view of diffraction plane (111) in (**a**)

After heat treatment, the periodic distribution feature of residual stress was eliminated. The absolute value of residual stress decreased with the increase in depth. The residual stress at the surface was compressive, reaching -127 MPa.

Schematics of residual stress evolution in the SLM and heat treatment process are shown in Fig. 8. The laser caused two typical zones in the current layer: fusion zone (FZ) and heat affected zone (HAZ). The laser beam irradiated and melted the powders to form the FZ, in which material was the stress-free molten liquid with a high temperature. Due to the heat conduction, the temperature in HAZ was increased, and thus the HAZ expansion occurred. Constrained by substrate mate-

rial, HAZ was in compressive stress state (Fig. 8a). When the laser was moved away, the molten liquid in FZ began to solidify. As the temperature decreased, the FZ shrinkage occurred, but FZ was constrained by HAZ, leading to the tensile stress in the FZ and higher compressive stress in HAZ (Fig. 8b). As the temperature further decreased to room temperature, the FZ contracted further. Therefore, a higher tensile stress existed in FZ, and a larger compressive stress in HAZ (Fig. 8c). During the heat treatment, the SLMed specimens were heated up in a furnace at 1175°C and held for one hour, and thus the residual stress was relieved to a certain extent at this elevated temperature (Fig. 8d). During the
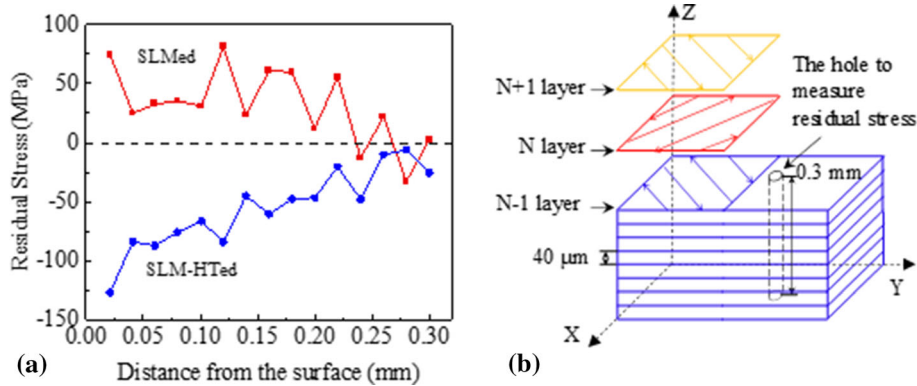
Fig. 7 (a) Surface residual stress in the specimen before and after heat treatment, (b) laser scanning strategy during the SLM process and hole drilling direction of residual stress measurement

water cooling process, temperature of the surface material was decreased rapidly, the shrinkage of the surface was constrained by the internal material, thereby the tensile stress was in the surface area; while the internal material was cooled slower and the extent of contraction was less, and thus compressive stress was in the subsurface area (Fig. 8e). As the temperature decreased further, the internal material continued to shrink, due to the constraint of the surface material, residual tensile stress was generated internally and compressive stress was generated in the surface, as shown in Fig. 8f.

### 3.3 Hardness and Tensile Properties Before and After Heat Treatment

Figure 9a-b shows the Vickers hardness and tensile test results of the specimens. The hardness of the SLMed and SLM-HTed specimens was 251 HV and 199 HV, respectively. The decrease in hardness of the SLM-HTed material is attributed to the exsolution of Cr and Mo at elevated temperature. Generally, continuous carbides on grain boundaries are harmful to the mechanical properties, but in this study, the carbides are discontinuously distributed, as shown in Fig. 4. Therefore, after the heat treatment, the ultimate tensile strength (UTS) remained unchanged, which was 235 MPa higher than that of the conventional forged specimens (Ref 25). The yield strength was decreased by 42%, due to the dissolution of the sub-grains, as shown in Fig. 3. Generally, the yield ratio (YR) is defined as the ratio of yield strength (YS) over UTS (Ref 16). A lower YR indicates a higher resistance to sudden fracture (Ref 26). The value of YR after heat treatment was reduced by 43%, which is beneficial to the fracture resistance of the material in the service condition. The elongation of the SLM-HTed material was increased by 53%, due to the lattice distortion reduction and the sub-grain dissolution during heat treatment. Fig. 9c-d shows the tensile fracture morphology of the specimens before and after heat treatment. The fracture surfaces showed a large number of dimples with typical plastic fracture characteristics, corresponding to the high fracture elongation of the SLM-HTed specimens in Fig. 9b. The average size of the dimples for the SLMed

specimen was around 0.5 μm (Fig. 9c), which was consistent with the sub-grain size in Fig. 3a. This was due to the fact that during the tensile test, dimples were formed inside the sub-grains, and several sub-grain boundaries were torn simultaneously. Therefore, cracks existed between the adjacent dimples, and the dimple's size was at the same level with that of the sub-grains. After heat treatment, sub-grains were dissolved (Fig. 3b), and a large number of interconnected dimples were formed in a matrix grain during the tensile process, so the SLM-HTed specimens had a higher elongation.

4. Conclusions

This paper focuses on the effect of heat treatment on the microstructure, mechanical properties, and residual stress of the GH3536 specimens manufactured by SLM. The following conclusions can be drawn:

(1) The heat treatment of the SLMed GH3536 reduced the degree of solid solution and led to the precipitation of Mo-rich carbides. Sub-grain boundaries of the SLMed specimens dissolved, and the degree of plastic deformation was reduced in the local area of the material after heat treatment.

(2) The residual tensile stress in the surface of the SLMed specimens converted to compressive stress of up to −127 MPa after heat treatment. The periodic distribution of subsurface residual stress disappeared.

(3) The hardness and yield strength of the SLMed specimens were decreased by 21 and 42% after heat treatment, respectively. It was mainly due to the reduction in solid solution strengthening and grain boundary strengthening. Fracture elongation was increased by 53% due to the lattice distortion reduction and the sub-grain dissolution during heat treatment.
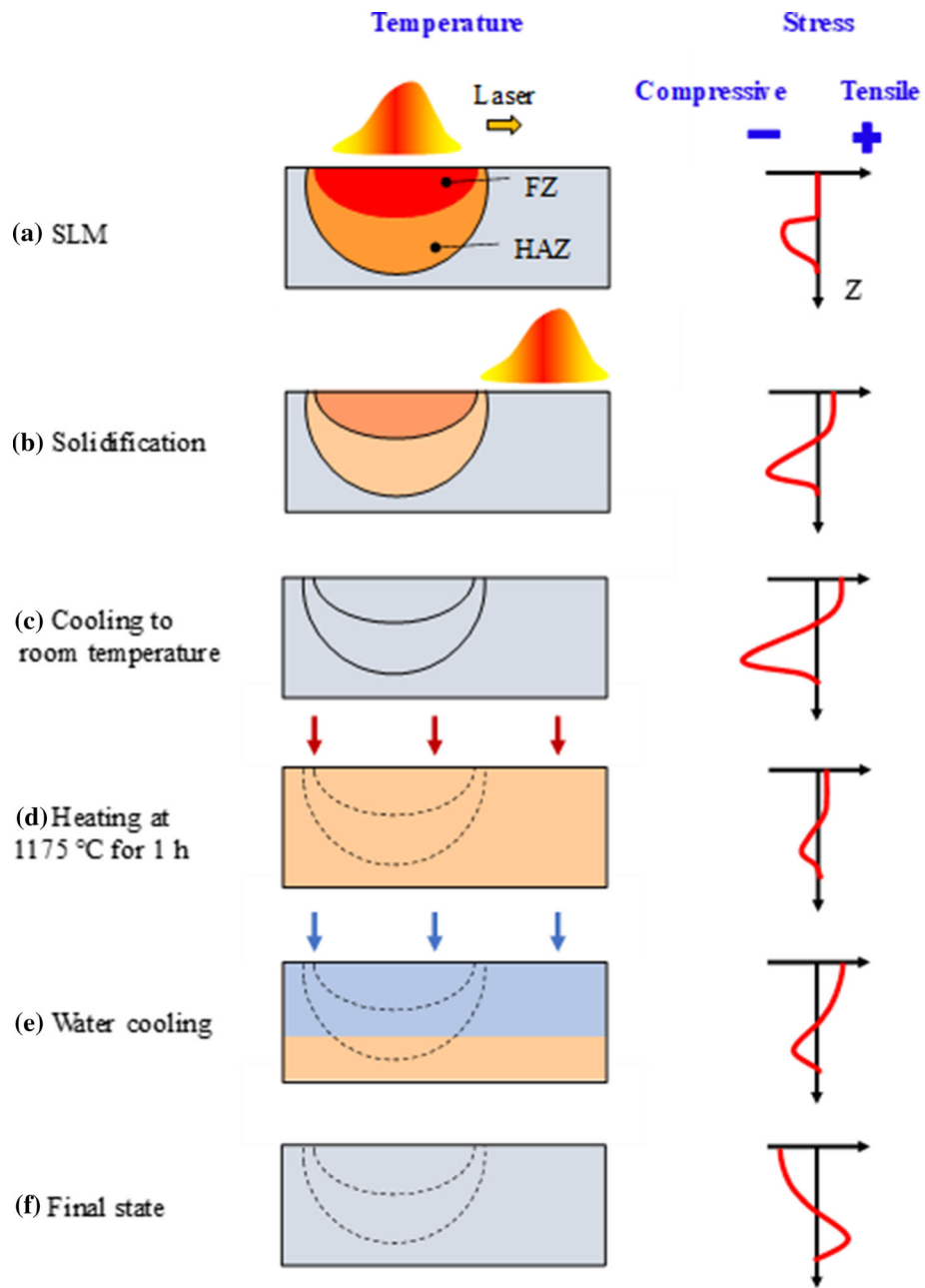
Fig. 8 Schematics of residual stress evolution of the SLMed (**a-c**) and SLM-HTed (**d-f**) specimens
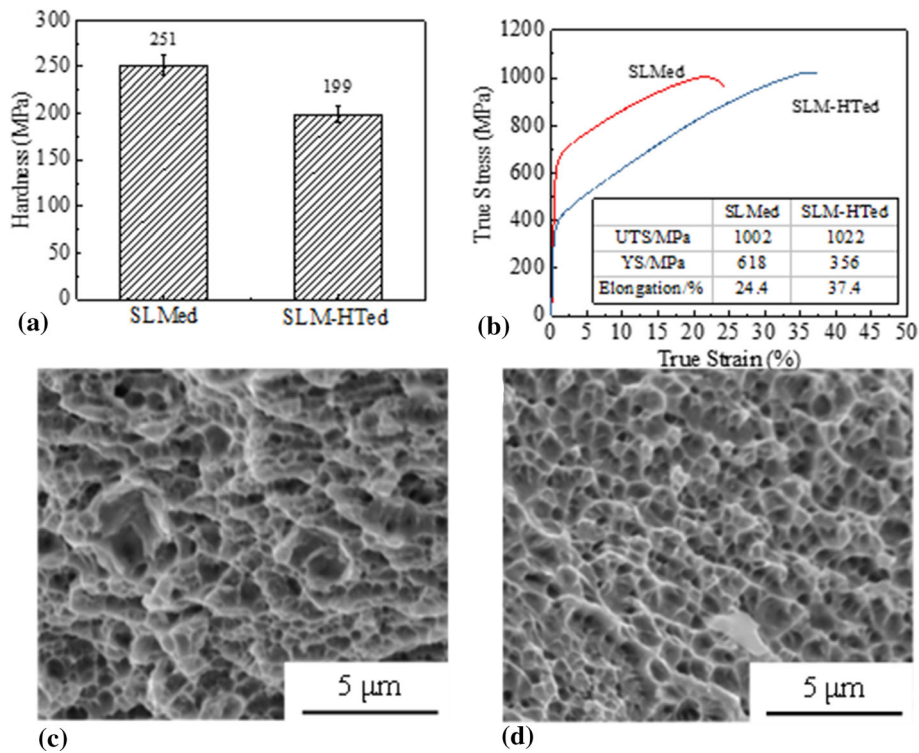
Fig. 9 (a) Hardness, (b) the true stress-true strain curve, and SEM images of fracture surfaces for (c) SLMed, (d) SLM-HTed specimens

Data Availability

The raw/processed data required to reproduce these findings cannot be shared at this time as the data also form part of an ongoing study.

Conflict of interest

The paper has no conflict of interest in any person or organization.

References

1. Y. Tian, D. Tomus, P. Rometsch and X. Wu, Influences of Processing Parameters on Surface Roughness of Hastelloy X Produced by Selective Laser Melting, *Addit. Manuf.*, 2017, **13**, p 103–112. https://doi.org/10.1016/j.addma.2016.10.010
2. H. Pirgazi, M. Sanjari, S. Tamimi, B. Shalchi Amirkhiz, L.A.I. Kestens and M. Mohammadi, Texture Evolution in Selective Laser Melted Maraging Stainless Steel CX with Martensitic Transformation, *J. Mater. Sci.*, 2021, **56**(1), p 844–853. https://doi.org/10.1007/s10853-020-05290-2
3. M.K. Gupta, A.K. Singla, H. Ji, Q. Song, Z. Liu, W. Cai, M. Mia, N. Khanna and G.M. Krolczyk, Impact of Layer Rotation on Microstructure, Grain size, Surface Integrity and Mechanical Behaviour of SLM Al-Si-10Mg Alloy, *J. Market. Res.*, 2020, **9**(5), p 9506–9522. https://doi.org/10.1016/j.jmrt.2020.06.090
4. Q. Han, Y. Gu, H. Gu, Y. Yin, J. Song, Z. Zhang and S. Soe, Laser Powder Bed Fusion of WC-reinforced Hastelloy-X Composite: Microstructure and Mechanical Properties, *J. Mater. Sci.*, 2021, **56**(2), p 1768–1782. https://doi.org/10.1007/s10853-020-05327-6
5. S. Abotula, A. Shukla and R. Chona, Dynamic Constitutive Behavior of Hastelloy X Under Thermo-mechanical Loads, *J. Mater. Sci.*, 2011, **46**(14), p 4971–4979. https://doi.org/10.1007/s10853-011-5414-y
6. M. Romedenne, R. Pillai, M. Kirka and S. Dryepondt, High Temperature Air Oxidation Behavior of Hastelloy X Processed by Electron Beam Melting (EBM) and Selective Laser Melting (SLM), *Corros. Sci.*, 2020, **171**, p 108647. https://doi.org/10.1016/j.corsci.2020.108647
7. Y. Yin, J. Zhang, J. Huo, K. Zhao, X. Zhu, X. Meng, Q. Han, Y. Ma, Z. Fu and J. Yin, Effect of Microstructure on the Passive Behavior of Selective Laser Melting-Fabricated Hastelloy X in NaNO3 Solution, *Mater. Charact.*, 2020, **165**, p 110370. https://doi.org/10.1016/j.matchar.2020.110370
8. K. Reuther, S. Hubig, I. Steinbach and M. Rettenmayr, Solute Trapping in Non-equilibrium Solidification: A Comparative Model Study, *Materialia*, 2019, **6**, p 100256. https://doi.org/10.1016/j.mtla.2019.100256
9. N.J. Harrison, I. Todd and K. Mumtaz, Reduction of Micro-cracking in Nickel Superalloys Processed by Selective Laser Melting: A Fundamental Alloy Design Approach, *Acta Mater.*, 2015, **94**, p 59–68. https://doi.org/10.1016/j.actamat.2015.04.035
10. X. Zhang, Z. Chai, H. Chen, J. Xu, L. Xu, H. Lu and X. Chen, A Novel Method to Prevent Cracking in Directed Energy Deposition of Inconel 738 by In-situ Doping Inconel 718, *Mater. Des.*, 2021, **197**, p 109214. https://doi.org/10.1016/j.matdes.2020.109214
11. X.Z. Qin, J.T. Guo, C. Yuan, J.S. Hou and H.Q. Ye, Precipitation and Thermal Instability of M23C6 Carbide in Cast Ni-base Superalloy K452, *Mater. Lett.*, 2008, **62**(2), p 258–261. https://doi.org/10.1016/j.matlet.2007.05.023
12. D. Tomus, Y. Tian, P.A. Rometsch, M. Heilmaier and X. Wu, Influence of Post Heat Treatments on Anisotropy of Mechanical Behaviour and Microstructure of Hastelloy-X Parts Produced by Selective Laser Melting, *Mater. Sci. Eng., A*, 2016, **667**, p 42–53. https://doi.org/10.1016/j.msea.2016.04.086
13. G. Marchese, E. Bassini, A. Aversa, M. Lombardi, D. Ugues, P. Fino and S. Biamino, Microstructural Evolution of Post-Processed Hastelloy X Alloy Fabricated by Laser Powder Bed Fusion, *Materials*, 2019, **12**(3), p 486. https://doi.org/10.3390/ma12030486

14. A. Keshavarzkermani, R. Esmaeilizadeh, P.D. Enrique, H. Asgari, N.Y. Zhou, A. Bonakdar and E. Toyserkani, Static Recrystallization Impact on Grain Structure and Mechanical Properties of Heat-Treated Hastelloy X Produced Via Laser Powder-Bed Fusion, *Mater. Charact.*, 2021, **173**, p 110969. https://doi.org/10.1016/j.matchar.2021.110969

15. M.L. Montero-Sistiaga, Z. Liu, L. Bautmans, S. Nardone, G. Ji, J.-P. Kruth, J. Van Humbeeck and K. Vanmeensel, Effect of Temperature on the Microstructure and Tensile Properties of Micro-crack Free Hastelloy X Produced by Selective Laser Melting, *Addit. Manuf.*, 2020, **31**, p 100995. https://doi.org/10.1016/j.addma.2019.100995

16. A.N. Jinoop, C.P. Paul and K.S. Bindra, Laser Assisted Direct Energy Deposition of Hastelloy-X, *Opt. Laser Technol.*, 2019, **109**, p 14–19. https://doi.org/10.1016/j.optlastec.2018.07.037

17. X. Zhang, H. Xu, Z. Li, A. Dong, D. Du, L. Lei, G. Zhang, D. Wang, G. Zhu and B. Sun, Effect of the Scanning Strategy on Microstructure and Mechanical Anisotropy of Hastelloy X Superalloy Produced by Laser Powder Bed Fusion, *Mater. Char.*, 2021, **173**, p 110951. https://doi.org/10.1016/j.matchar.2021.110951

18. X. Wang and K. Chou, The Effects of Stress Relieving Heat Treatment on the Microstructure and Residual Stress of Inconel 718 Fabricated by Laser Metal Powder Bed Fusion Additive Manufacturing Process, *J. Manuf. Process.*, 2019, **48**, p 154–163. https://doi.org/10.1016/j.jmapro.2019.10.027

19. G. Kasperovich, J. Haubrich, J. Gussone and G. Requena, Correlation Between Porosity and Processing Parameters in TiAl6V4 Produced by Selective Laser Melting, *Mater. Des.*, 2016, **105**, p 160–170. https://doi.org/10.1016/j.matdes.2016.05.070

20. S.A. Khairallah, A.T. Anderson, A. Rubenchik and W.E. King, Laser Powder-Bed Fusion Additive Manufacturing: Physics of Complex Melt Flow and Formation Mechanisms of Pores, Spatter, and Denudation Zones, *Acta Mater.*, 2016, **108**, p 36–45. https://doi.org/10.1016/j.actamat.2016.02.014

21. S. Li, Q. Wei, Y. Shi, Z. Zhu and D. Zhang, Microstructure Characteristics of Inconel 625 Superalloy Manufactured by Selective Laser Melting, *J. Mater. Sci. Technol.*, 2015, **31**(9), p 946–952. https://doi.org/10.1016/j.jmst.2014.09.020

22. H.M. Tawancy, Long-term Ageing Characteristics of Hastelloy Alloy X, *J. Mater. Sci.*, 1983, **18**(10), p 2976–2986. https://doi.org/10.1007/BF00700780

23. J.S. Weaver, V. Livescu and N.A. Mara, A Comparison of Adiabatic Shear Bands in Wrought and Additively Manufactured 316L Stainless Steel Using Nanoindentation and Electron Backscatter Diffraction, *J. Mater. Sci.*, 2020, **55**(4), p 1738–1752. https://doi.org/10.1007/s10853-019-03994-8

24. Y. Liu, Y. Yang and D. Wang, A Study on the Residual Stress During Selective Laser Melting (SLM) of Metallic Powder, *Int. J. Adv. Manuf. Technol.*, 2016, **87**(1), p 647–656. https://doi.org/10.1007/s00170-016-8466-y

25. F. Wang, X.H. Wu and D. Clark, On Direct Laser Deposited Hastelloy X: Dimension, Surface Finish, Microstructure and Mechanical Properties, *Mater. Sci. Technol.*, 2011, **27**(1), p 344–356. https://doi.org/10.1179/026708309X12578491814591

26. X. Li, Y. Liu, K. Gan, J. Dong and C. Liu, Acquiring a Low Yield Ratio Well Synchronized with Enhanced Strength of HSLA Pipeline Steels Through Adjusting Multiple-Phase Microstructures, *Mater. Sci. Eng., A*, 2020, **785**, p 139350. https://doi.org/10.1016/j.msea.2020.139350